

# Layer Hall effect induced by altermagnetism

Fang Qin<sup>1,\*</sup> and Rui Chen<sup>2,†</sup>

<sup>1</sup>*School of Science, Jiangsu University of Science and Technology, Zhenjiang, Jiangsu 212100, China*

<sup>2</sup>*Department of Physics, Hubei University, Wuhan, Hubei 430062, China*

In this work, we propose a scheme to realize the layer Hall effect in the ferromagnetic topological insulator  $\text{Bi}_2\text{Se}_3$  via proximity to  $d$ -wave altermagnets. We show that an altermagnet and an in-plane magnetic field applied near one surface gap the corresponding Dirac cone, yielding an altermagnet-induced half-quantized Hall effect. When altermagnets with antiparallel Néel vectors are placed near the top and bottom surfaces, giving rise to the layer Hall effect with vanishing net Hall conductance, i.e., the altermagnet-induced layer Hall effect. In contrast, altermagnets with parallel Néel vectors lead to a quantized Chern insulating state, i.e., the altermagnet-induced anomalous Hall effect. We further analyze the dependence of the Hall conductance on the orientation of the in-plane magnetic field and demonstrate that the layer Hall effect becomes observable under a perpendicular electric field. Our results establish a route to engineer altermagnet-induced topological phases in ferromagnetic topological insulators.

## I. INTRODUCTION

The layer Hall effect describes a distinctive electronic response in which charge carriers are spontaneously deflected toward opposite transverse sides in different atomic layers [1–14]. This phenomenon has been experimentally observed in even-layered antiferromagnetic topological insulators such as  $\text{MnBi}_2\text{Te}_4$  [1], marking a major milestone in the exploration of layer-resolved Hall responses. Theoretically, the concept has been extended to a variety of material platforms, including  $\text{MnBi}_2\text{Te}_4$ ,  $\text{In}_2\text{Se}_3$ , and  $\text{In}_2\text{Te}_3$  heterostructures [1–7], transition-metal oxides [8], magnetic sandwich heterostructures [9], valleytronic van der Waals bilayers [10], inversion-symmetric monolayers [11], and multiferroic materials [12, 13].

In most cases, the layer Hall effect arises from an externally applied electric field [1, 2, 4, 8–10], although similar responses can also be induced by internal electric fields generated through ferroelectric polarization [6, 13] or interlayer sliding [5, 10, 12]. Beyond electric-field-driven mechanisms, a distinct route has been proposed in which inequivalent exchange fields applied to the top and bottom surfaces of a topological-insulator thin film produce a spontaneous layer Hall effect, even without external bias [14]. Importantly, the layer Hall effect has also been recognized as a key experimental signature of the axion insulator phase [9, 15–27], providing a crucial connection between magnetic symmetry breaking and topological electromagnetic responses.

Altermagnetism represents a recently identified class of collinear magnetic phases distinguished by unique spin-group symmetries [28–35]. Altermagnets exhibit anisotropic spin-split electronic bands and alternating collinear magnetic moments on adjacent lattice sites, setting them apart from conventional ferromag-

nets and antiferromagnets [28–35]. A rapidly expanding list of candidate altermagnetic materials includes  $\text{RuO}_2$  [35–43],  $\text{RuF}_4$  [44],  $\text{ReO}_2$  [45],  $\text{MnF}_2$  [46, 47],  $\text{FeSb}_2$  [48–50],  $\text{CrSb}$  [51–54],  $\text{MnTe}$  [55–59],  $\text{Mn}_5\text{Si}_3$  [60–62],  $(\text{Ca},\text{Ce})\text{MnO}_3$  [63, 64], and  $\text{KV}_2\text{Se}_2\text{O}$  [65, 66].

A variety of experimental schemes have been proposed to detect altermagnetism [67–69]. Coulomb drag has been identified as a possible probe of altermagnetic order [67], while electrical switching of altermagnetic states has been theoretically demonstrated [68]. Experimental setups for directly probing momentum-space spin polarization [69] and distinguishing intrinsic from extrinsic spin-orbital altermagnetism via spin conductivity and orbital polarization [70] have also been suggested.

Theoretical studies have revealed a wide range of unconventional phenomena in altermagnets, including the Josephson effect [71–75], Andreev reflection [76, 77], nonlinear transport [78, 79], magnetoresistance effect [80], parity anomaly [81], helical edge states [82], quasicrystals [83–85], and Néel spin currents [86]. Additionally, numerous topological effects have been predicted, such as altermagnet-induced topological phases [64, 87–91], higher-order topological states [47], floating edge bands [92], light-induced odd-parity altermagnetism [93–96], Floquet-engineered topological phases [97], and topological superconductivity [98]. These developments position altermagnetism as a promising platform for engineering and controlling topological and correlated quantum phases.

In this work, we propose a scheme to realize the layer Hall effect in the ferromagnetic topological insulator  $\text{Bi}_2\text{Se}_3$  via proximity to  $d$ -wave altermagnets. We consider a three-dimensional (3D) ferromagnetic topological insulator coupled to altermagnetic layers under an external in-plane layer magnetic field. We find that inserting an altermagnet and applying an in-plane magnetic field to layers near either the top or bottom surface opens a gap in the corresponding surface Dirac cone, giving rise to an altermagnet-induced half-quantized Hall effect as shown in Figs. 1(a) and 1(b). Specifically:

\* [qinfang@just.edu.cn](mailto:qinfang@just.edu.cn)

† [chenr@hubu.edu.cn](mailto:chenr@hubu.edu.cn)

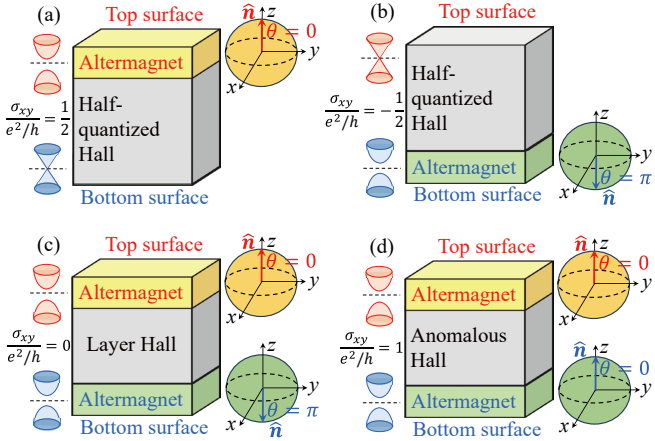


FIG. 1. Schematic of topological phases in a three-dimensional topological insulator  $\text{Bi}_2\text{Se}_3$  in the presence of  $d$ -wave altermagnetic order on the top or bottom layers. The unit vector  $\hat{\mathbf{n}} = (\sin \theta \cos \phi, \sin \theta \sin \phi, \cos \theta)$  denotes the orientation of the Néel vector [38, 47], where  $\theta$  and  $\phi$  are the polar and azimuthal angles, respectively. For simplicity,  $\theta=0$  or  $\pi$ . (a) Altermagnet penetrating only the top layers (yellow) gaps the top surface Dirac cone via time-reversal-symmetry breaking, giving rise to an altermagnet-induced half-quantized Hall effect. (b) Altermagnet penetrating only the bottom layers (green) gaps the bottom surface Dirac cone, leading to a half-quantized Hall effect. (c) Antiparallel Néel vectors on the top and bottom surfaces gap both Dirac cones with opposite Hall contributions, resulting in an altermagnet-induced layer Hall effect with zero net Hall conductance. (d) Parallel Néel vectors on the two surfaces gap both Dirac cones with identical Hall contributions, yielding an altermagnet-induced anomalous Hall effect and a fully quantized Chern insulating phase.

- When altermagnets with antiparallel Néel vectors [38, 47] are placed near the top and bottom surfaces, both Dirac cones become gapped with opposite Hall contributions, producing the altermagnet-induced layer Hall effect with vanishing net Hall conductance as shown in Fig. 1(c).
- When altermagnets with parallel Néel vectors are applied to both surfaces, the two Dirac cones become gapped with the same Dirac mass, yielding a fully quantized Chern insulating state, i.e., the altermagnet-induced anomalous Hall effect as shown in Fig. 1(d).

Furthermore, we investigate the dependence of the Hall conductance on the orientation of the in-plane magnetic field and demonstrate that the layer Hall effect becomes experimentally accessible under a perpendicular electric field. Our results establish a versatile strategy for realizing altermagnet-induced topological phases in ferromagnetic topological insulators, paving the way toward the design and implementation of altermagnet-based topological materials.

The remainder of the paper is organized as follows. Section II introduces the model Hamiltonian for the 3D

$\mathbb{Z}_2$  topological insulator  $\text{Bi}_2\text{Se}_3$  coupled to altermagnetic layers under an in-plane layer magnetic field. Section III presents numerical results for  $d$ -wave altermagnets. In Section IV, we derive the effective surface Hamiltonians and analytically obtain the Hall conductances. In Section V, we show how a perpendicular electric field can be used to reveal the layer Hall effect. Finally, Section VI summarizes the main conclusions.

## II. MODEL

We investigate a 3D  $\mathbb{Z}_2$  topological insulator,  $\text{Bi}_2\text{Se}_3$ , placed in proximity to altermagnetic layers and subjected to an external in-plane layer magnetic field. The corresponding low-energy effective Hamiltonian is written as

$$\hat{\mathcal{H}}(\mathbf{k}) = \hat{\mathcal{H}}_{\text{TI}}(\mathbf{k}) + \hat{\mathcal{H}}_{\Delta} + \hat{\mathcal{H}}_J(\mathbf{k}_{||}), \quad (1)$$

where  $\mathbf{k} = (k_x, k_y, k_z)$  and  $\mathbf{k}_{||} = (k_x, k_y)$ . The three terms represent, respectively, the bulk Hamiltonian of  $\text{Bi}_2\text{Se}_3$ , the Zeeman-type spin splitting induced by magnetic doping, and the momentum-dependent altermagnetic exchange coupling arising from proximity to altermagnetic layers.

The first term,  $\hat{\mathcal{H}}_{\text{TI}}(\mathbf{k})$ , describes the bulk electronic structure of  $\text{Bi}_2\text{Se}_3$  and takes the standard form [99]

$$\hat{\mathcal{H}}_{\text{TI}}(\mathbf{k}) = \mathcal{M}(\mathbf{k})\sigma_0 \otimes \tau_z + A_1 k_z \sigma_0 \otimes \tau_y + A_2 (k_y \sigma_x - k_x \sigma_y) \otimes \tau_x, \quad (2)$$

where  $\mathcal{M}(\mathbf{k}) = M - B_1 k_z^2 - B_2 (k_x^2 + k_y^2)$ , and  $\sigma_{x,y,z}$  ( $\tau_{x,y,z}$ ) are Pauli matrices acting on spin (orbital) degrees of freedom. The material parameters are chosen as  $M = 0.28$  eV,  $A_1 = 0.22$  eV·nm,  $A_2 = 0.41$  eV·nm,  $B_1 = 0.10$  eV·nm<sup>2</sup>, and  $B_2 = 0.566$  eV·nm<sup>2</sup>, consistent with the well-established model of  $\text{Bi}_2\text{Se}_3$  [26, 69, 99–104].

The second term,  $\hat{\mathcal{H}}_{\Delta} = F(z)(\Delta_x \sigma_y - \Delta_y \sigma_x) \otimes \tau_0$ , represents a Zeeman-type spin splitting arising from the exchange field induced by magnetic doping [99, 105]. Here,  $\Delta_x = \Delta \cos \varphi$  and  $\Delta_y = \Delta \sin \varphi$ , where  $\Delta$  denotes the magnitude of the exchange field [101, 106, 107] and  $\varphi$  specifies the in-plane orientation angle of the applied magnetic field. The function  $F(z)$  captures the spatial profile of the magnetic proximity effect along the  $z$  direction, ensuring that the induced magnetization is localized near the surface or interface [102].

The third term,  $\hat{\mathcal{H}}_J(\mathbf{k}_{||}) = G(z)J(k_x, k_y)\sigma_z \otimes \tau_0$ , describes the contribution from altermagnetic ordering induced by the adjacent altermagnetic layers. The function  $J(k_x, k_y)$  encodes the momentum-dependent form factor associated with the altermagnetic order, while  $G(z)$  characterizes the spatial dependence of this interfacial coupling. Furthermore, we consider a  $d$ -wave altermagnetic term of the form  $\hat{\mathcal{H}}_J(\mathbf{k}_{||}) = G(z)J_d(k_y^2 - k_x^2)(\boldsymbol{\sigma} \cdot \hat{\mathbf{n}}) \otimes \tau_0 = G(z)J_d(k_y^2 - k_x^2) \cos \theta \sigma_z \otimes \tau_0$  [32–34], where the unit vector  $\hat{\mathbf{n}} = (\sin \theta \cos \phi, \sin \theta \sin \phi, \cos \theta)$  denotes the direction of the Néel vector [47], with  $\theta$  and  $\phi$  being the polar and

azimuthal angles in spherical coordinates, respectively. To realize the layer Hall effect, we set  $\theta=0$  for the top surface states and  $\theta=\pi$  for the bottom surface states, as illustrated in Fig. 1(c). In contrast, the anomalous Hall effect is obtained by choosing  $\theta=0$  for both the top and bottom surface states, as shown in Fig. 1(d).

Together, these three components capture the essential physics of a ferromagnetic topological insulator in proximity to altermagnetic layers, providing the basis for exploring the emergence of the altermagnet-induced layer Hall effect.

### III. NUMERICAL RESULTS

We now present numerical results for the  $d$ -wave altermagnets. The altermagnetic strength is chosen to be of the same order as the quadratic term in  $\text{Bi}_2\text{Se}_3$ , i.e.,  $J_d=B_2$ .

#### A. Tight-binding Hamiltonian

To perform the numerical calculations, we map the continuum Hamiltonian (1) onto its tight-binding form in momentum space (see Sec. SII A of the Supplemental Material [108]):

$$\hat{\mathcal{H}}_{\text{TB}}(\mathbf{k})=\hat{\mathcal{H}}_{\text{TI}}^{\text{TB}}(\mathbf{k})+\hat{\mathcal{H}}_{\Delta}+\hat{\mathcal{H}}_J^{\text{TB}}(\mathbf{k}_{||}), \quad (3)$$

where

$$\begin{aligned} \hat{\mathcal{H}}_{\text{TI}}^{\text{TB}}(\mathbf{k}) &= \mathcal{M}_{\text{TB}}(\mathbf{k})\sigma_0\otimes\tau_z+\lambda_z\sin(k_za_z)\sigma_0\otimes\tau_y \\ &+ \lambda_{||}\sin(k_ya_{||})\sigma_x\otimes\tau_x \\ &- \lambda_{||}\sin(k_xa_{||})\sigma_y\otimes\tau_x, \end{aligned} \quad (4)$$

$$\begin{aligned} \mathcal{M}_{\text{TB}}(\mathbf{k}) &= (M-2t_z-4t_{||})+2t_z\cos(k_za_z) \\ &+ 2t_{||}[\cos(k_xa_{||})+\cos(k_ya_{||})], \end{aligned} \quad (5)$$

$$\hat{\mathcal{H}}_J^{\text{TB}}(\mathbf{k}_{||})=2G(z)J_{||}\cos\theta[\cos(k_xa_{||})-\cos(k_ya_{||})]\sigma_z\otimes\tau_0. \quad (6)$$

The parameters are defined as  $t_z=B_1/a_z^2$ ,  $t_{||}=B_2/a_{||}^2$ ,  $\lambda_z=A_1/a_z$ ,  $\lambda_{||}=A_2/a_{||}$ , and  $J_{||}=J_d/a_{||}^2$ , with  $a_x=a_y=a_{||}$  denoting the lattice constants.

Under open boundary conditions (OBCs) along the  $z$  direction and periodic boundary conditions (PBCs) along  $x$  and  $y$  directions, the real-space tight-binding Hamiltonian in the basis  $(\hat{C}_{k_x,k_y,1}, \hat{C}_{k_x,k_y,2}, \hat{C}_{k_x,k_y,3}, \dots, \hat{C}_{k_x,k_y,N_z})^T$  is given

by (see Sec. SII B of the Supplemental Material [108])

$$\hat{\mathcal{H}}_{\text{TB}}(\mathbf{k}_{||})=\begin{pmatrix} \hat{h}(\mathbf{k}_{||}) & \hat{T}_z & 0 & \cdots & 0 \\ \hat{T}_z^\dagger & \hat{h}(\mathbf{k}_{||}) & \hat{T}_z & \cdots & 0 \\ 0 & \hat{T}_z^\dagger & \hat{h}(\mathbf{k}_{||}) & \ddots & \vdots \\ \vdots & \ddots & \ddots & \ddots & \hat{T}_z \\ 0 & \cdots & 0 & \hat{T}_z^\dagger & \hat{h}(\mathbf{k}_{||}) \end{pmatrix}_{(4N_z)\times(4N_z)}, \quad (7)$$

where

$$\begin{aligned} \hat{h}(\mathbf{k}_{||}) &= \hat{M}_0+\hat{T}_x e^{ik_x a_{||}}+\hat{T}_x^\dagger e^{-ik_x a_{||}} \\ &+ \hat{T}_y e^{ik_y a_{||}}+\hat{T}_y^\dagger e^{-ik_y a_{||}}, \end{aligned} \quad (8)$$

$$\begin{aligned} \hat{M}_0 &= (M-2t_z-4t_{||})\sigma_0\otimes\tau_z \\ &+ F(z)(\Delta_x\sigma_y-\Delta_y\sigma_x)\otimes\tau_0, \end{aligned} \quad (9)$$

$$\hat{T}_z=t_z\sigma_0\otimes\tau_z-i\frac{\lambda_z}{2}\sigma_0\otimes\tau_y, \quad (10)$$

$$\hat{T}_z^\dagger=t_z\sigma_0\otimes\tau_z+i\frac{\lambda_z}{2}\sigma_0\otimes\tau_y, \quad (11)$$

$$\begin{aligned} \hat{T}_x &= t_{||}\sigma_0\otimes\tau_z+i\frac{\lambda_{||}}{2}\sigma_y\otimes\tau_x+G(z)J_{||}\cos\theta\sigma_z\otimes\tau_0, \quad \hat{T}_x^\dagger=t_{||}\sigma_0\otimes\tau_z-i\frac{\lambda_{||}}{2}\sigma_y\otimes\tau_x+G(z)J_{||}\cos\theta\sigma_z\otimes\tau_0, \quad \hat{T}_y=t_{||}\sigma_0\otimes\tau_z-i\frac{\lambda_{||}}{2}\sigma_x\otimes\tau_x-G(z)J_{||}\cos\theta\sigma_z\otimes\tau_0, \quad \text{and} \quad \hat{T}_y^\dagger=t_{||}\sigma_0\otimes\tau_z+i\frac{\lambda_{||}}{2}\sigma_x\otimes\tau_x-G(z)J_{||}\cos\theta\sigma_z\otimes\tau_0. \end{aligned}$$

#### B. Topological phases

Figure 2 displays the band structures and Hall conductances for the tight-binding Hamiltonian (7) of  $\text{Bi}_2\text{Se}_3$  coupled to  $d$ -wave altermagnetic layers under an external in-plane magnetic field. To elucidate the distinct roles of the altermagnet and the external field, we summarize the resulting topological phases below, referring directly to Fig. 2.

- Figures 2(a1) and 2(a2): Altermagnet-induced half-quantized Hall effect. The top-surface Dirac cone is gapped by the altermagnet, while the bottom-surface Dirac cone remains gapless [Fig. 2(a1)]. This yields a positive half-quantized Hall conductance [Fig. 2(a2)], with the plateau width determined by the surface gap. Here,  $\theta=0$ ,  $F(z)=G(z)=1$  for  $0\leq z\leq 2$  nm and  $F(z)=G(z)=0$  elsewhere. The sample thickness along the  $z$  direction is  $L_z=10$  nm.
- Figures 2(b1) and 2(b2): Altermagnet-induced half-quantized Hall effect (opposite sign). When the altermagnet acts only on the bottom layers

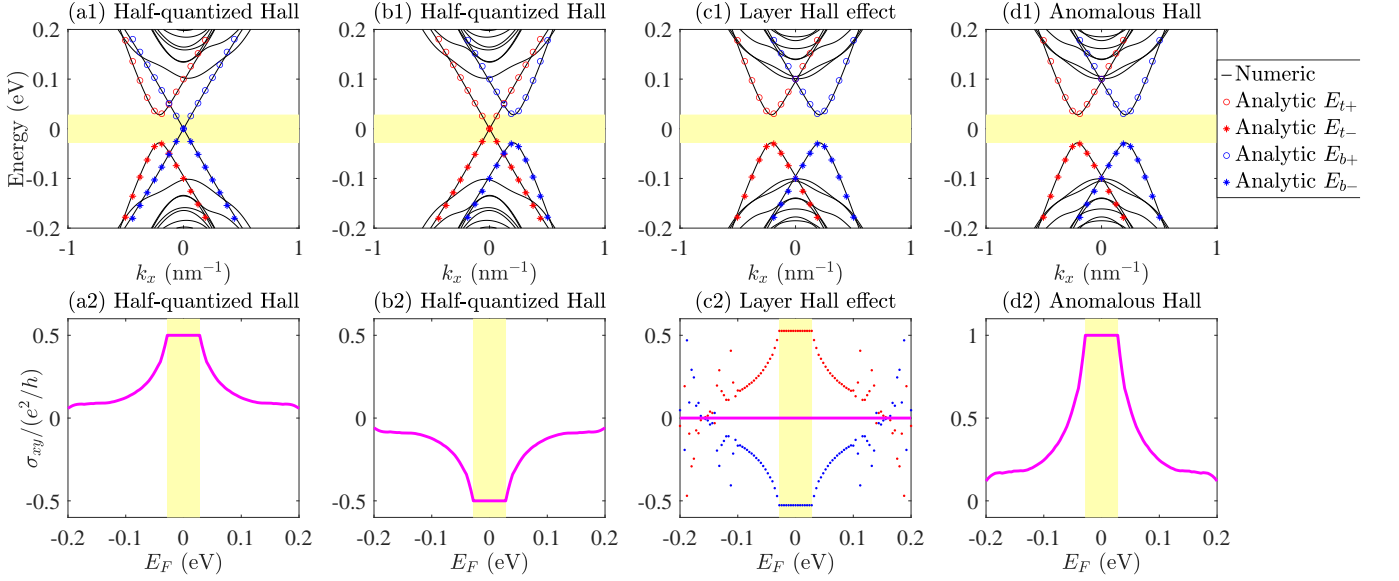


FIG. 2. Band structures and Hall conductances for the tight-binding Hamiltonian (7) of  $\text{Bi}_2\text{Se}_3$  in proximity to  $d$ -wave altermagnetic layers under an external in-plane magnetic field. [(a1)-(d1)] Energy spectra. Black curves show numerical results obtained under OBCs along  $z$  direction and PBCs along  $x$  and  $y$  directions. Red (blue) circles and asterisks denote the analytical surface-state spectra for the top (bottom) surface, derived from Eqs. (13) and (15). Subscripts label the surface bands:  $t+$  (top conduction),  $t-$  (top valence),  $b+$  (bottom conduction), and  $b-$  (bottom valence). (a1) Top-surface altermagnetic layer with thickness  $d_t = 2$  nm, which gaps the top Dirac cone. Here,  $\theta = 0$ ,  $G(z) \cos 0 = F(z) = 1$  for  $0 \leq z \leq 2$  nm and  $G(z) = F(z) = 0$  elsewhere. (b1) Bottom-surface inverse altermagnetic layer with thickness  $d_b = 2$  nm, which gaps the bottom Dirac cone. Here,  $\theta = \pi$ ,  $G(z) \cos \pi = -F(z) = -1$  for  $8 \leq z \leq 10$  nm and  $G(z) = F(z) = 0$  elsewhere. (c1) Combined top altermagnetic layer ( $d_t = 2$  nm) and bottom inverse altermagnetic layer ( $d_b = 2$  nm), which gap both surface Dirac cones. Here,  $G(z) \cos 0 = F(z) = 1$  for  $0 \leq z \leq 2$  nm,  $G(z) \cos \pi = -F(z) = -1$  for  $8 \leq z \leq 10$  nm, and  $G(z) = F(z) = 0$  elsewhere. (d1) Top and bottom altermagnetic layers with parallel Néel vectors,  $d_t = d_b = 2$  nm and  $\theta = 0$ , simultaneously gap both surfaces. Here,  $G(z) \cos 0 = F(z) = 1$  for  $0 \leq z \leq 2$  nm and  $8 \leq z \leq 10$  nm, and  $G(z) = F(z) = 0$  elsewhere. Yellow shaded regions indicate the bandwidths of the corresponding surface states. [(a2)-(d2)] Hall conductance as a function of the Fermi energy  $E_F$  for the configurations in (a1)-(d1), exhibiting positive half-quantized, negative half-quantized, vanishing, and integer-quantized values in the energy gaps, respectively. In (c2), red (blue) dots represent the summed layer Hall conductance of the top (bottom) two layers. Other parameters:  $M = 0.28$  eV,  $A_1 = 0.22$  eV·nm,  $A_2 = 0.41$  eV·nm,  $B_1 = 0.1$  eV·nm $^2$ ,  $B_2 = 0.566$  eV·nm $^2$ ,  $\Delta = 0.1$  eV,  $J_d = B_2$ ,  $\varphi = 0$ ,  $a_z = a_{||} = 1$  nm, and sample thickness  $L_z = 10$  nm along the  $z$  direction.

$[\theta = \pi$  and  $G(z) = 1]$ , the bottom-surface Dirac cone is gapped while the top surface remains gapless [Fig. 2(b1)]. This configuration produces a negative half-quantized Hall conductance [Fig. 2(b2)], again with a plateau width determined by the gapped bandwidth. The sign reversal of the Hall conductance arises from  $G(z) \cos \theta = -1$  with  $\theta = \pi$  and  $G(z) = 1$  in the bottom layers, contrasting with the positive value in Fig. 2(a2).

- Figures 2(c1) and 2(c2): Altermagnet-induced layer Hall effect. Both the top and bottom Dirac cones are gapped by altermagnets with antiparallel Néel vectors [Fig. 2(c1)], with  $G(z) \cos 0 = F(z) = 1$  for  $0 \leq z \leq 2$  nm and  $G(z) \cos \pi = -F(z) = -1$  for  $8 \leq z \leq 10$  nm. The resulting Hall conductances on the two surfaces cancel, giving zero net Hall response, as seen in Fig. 2(c2). Red (blue) dots indicate the summed Hall conductance from the top (bottom) two layers, and the width of the quantized plateau of the summed layer Hall con-

ductance is determined by the gapped bandwidth.

- Figures 2(d1) and 2(d2): Altermagnet-induced anomalous Hall effect (Chern insulator). When both the top and bottom altermagnetic layers have the same sign of  $G(z)$ , both Dirac cones are gapped with identical sign [Fig. 2(d1)], resulting in a quantized Chern insulating state with total Hall conductance  $e^2/h$  [Fig. 2(d2)], and the width of the quantized plateau is determined by the gapped bandwidth.

In Figs. 2(a1)-2(d1), the numerical spectra (black curves) obtained under OBCs along  $z$  direction and PBCs along  $x$ ,  $y$  directions agree with the analytical surface-state dispersions [Eqs. (13) and (15)], shown in red (top surface) and blue (bottom surface). The bands are labeled as “ $t+$ ” (top-surface conduction), “ $t-$ ” (top-surface valence), “ $b+$ ” (bottom-surface conduction), and “ $b-$ ” (bottom-surface valence).

#### IV. SURFACE STATES

In this section, we present the effective Hamiltonians and corresponding eigenenergies for the surface states, and analytically derive the associated Hall conductances.

The effective Hamiltonian for the top surface state is given by (see Section SIII C of the Supplemental Material [108]),

$$\hat{\mathcal{H}}_{\text{sur}}^{\text{top}}(\mathbf{k}_{||}) = -A_2 \left( k_y + \frac{\Delta_y}{A_2} \right) \sigma_x + A_2 \left( k_x + \frac{\Delta_x}{A_2} \right) \sigma_y + J_{\text{top}}(k_x, k_y) \sigma_z. \quad (12)$$

The corresponding eigenenergies for the top surface states are

$$E_{\text{sur}}^{\text{top}(\pm)}(\mathbf{k}_{||}) = \pm \sqrt{A_2^2 [E_0^{\text{top}}(k_x, k_y)]^2 + [J_{\text{top}}(k_x, k_y)]^2}, \quad (13)$$

$$\text{where } [E_0^{\text{top}}(k_x, k_y)]^2 = \left( k_y + \frac{\Delta_y}{A_2} \right)^2 + \left( k_x + \frac{\Delta_x}{A_2} \right)^2.$$

Similarly, the effective Hamiltonian for the bottom surface state is obtained as (see Section SIII C of the Supplemental Material [108])

$$\hat{\mathcal{H}}_{\text{sur}}^{\text{bot}}(\mathbf{k}_{||}) = A_2 \left( k_y - \frac{\Delta_y}{A_2} \right) \sigma_x - A_2 \left( k_x - \frac{\Delta_x}{A_2} \right) \sigma_y + J_{\text{bot}}(k_x, k_y) \sigma_z. \quad (14)$$

The corresponding eigenenergies are

$$E_{\text{sur}}^{\text{bot}(\pm)}(\mathbf{k}_{||}) = \pm \sqrt{A_2^2 [E_0^{\text{bot}}(k_x, k_y)]^2 + [J_{\text{bot}}(k_x, k_y)]^2}, \quad (15)$$

$$\text{where } [E_0^{\text{bot}}(k_x, k_y)]^2 = \left( k_y - \frac{\Delta_y}{A_2} \right)^2 + \left( k_x - \frac{\Delta_x}{A_2} \right)^2.$$

##### A. Hall conductance versus magnetic-field orientation

Based on the effective Hamiltonians (12) and (14), we consider a  $d$ -wave altermagnetic term  $\hat{\mathcal{H}}_J(\mathbf{k}_{||}) = G(z) J_d(k_y^2 - k_x^2) \cos \theta \sigma_z \otimes \tau_0$  [32–34]. The Hall conductances for the surface states can then be obtained analytically as (see Section SIV of the Supplemental Material [108])

$$\sigma_{xy}^{\text{top}} = \frac{e^2}{2h} \int \frac{J_+ G(z) \cos \theta}{\{d_+^2 + J_{\text{sur}}^2 [G(z) \cos \theta]^2\}^{3/2}} \frac{dk_x dk_y}{2\pi}, \quad (16)$$

$$\sigma_{xy}^{\text{bot}} = \frac{e^2}{2h} \int \frac{J_- G(z) \cos \theta}{\{d_-^2 + J_{\text{sur}}^2 [G(z) \cos \theta]^2\}^{3/2}} \frac{dk_x dk_y}{2\pi}, \quad (17)$$

$$\text{where } J_{\pm} = A_2^2 J_d \left[ k_y \left( k_y \pm 2 \frac{\Delta_y}{A_2} \right) - k_x \left( k_x \pm 2 \frac{\Delta_x}{A_2} \right) \right], \quad d_{\pm} = \left\{ A_2^2 \left[ \left( k_y \pm \frac{\Delta_y}{A_2} \right)^2 + \left( k_x \pm \frac{\Delta_x}{A_2} \right)^2 \right] \right\}^{1/2}, \quad J_{\text{sur}} = J_d (k_y^2 - k_x^2),$$

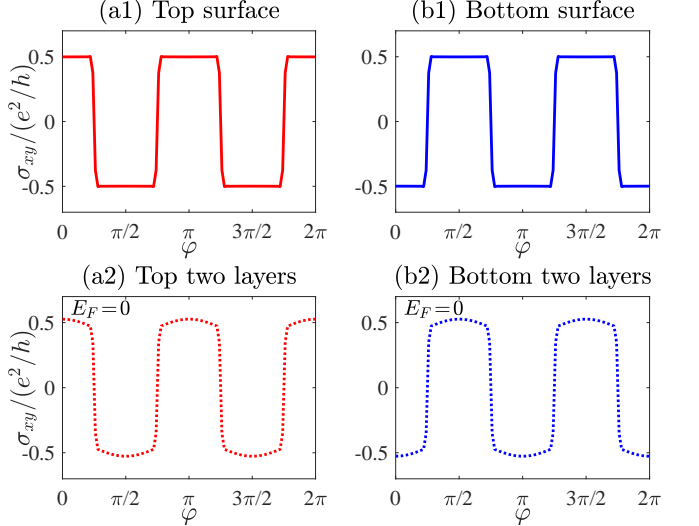


FIG. 3. Upper row: [(a1), (b1)] Hall conductances of the top and bottom surfaces as functions of the angle  $\varphi$ , calculated from the analytical expressions in Eqs. (16) and (17), respectively. (a1) Top-surface Hall conductance with  $\theta = 0$  and  $G(z) \cos 0 = F(z) = 1$ . (b1) Bottom-surface Hall conductance with  $\theta = \pi$  and  $G(z) \cos \pi = -F(z) = -1$ . Here,  $\varphi$  specifies the orientation of the external in-plane magnetic field. The integration range is  $k_x, k_y \in [-\pi, \pi] \text{ nm}^{-1}$ , and the Fermi energy  $E_F$  is set within the surface-state gap. Lower row: [(a2), (b2)] Summed layer Hall conductance of the top (bottom) two layers as a function of  $\varphi$ , for a system with both a top altermagnetic layer ( $d_t = 2 \text{ nm}$ ) and a bottom inverse altermagnetic layer ( $d_b = 2 \text{ nm}$ ). The spatial profiles are given by  $G(z) \cos 0 = F(z) = 1$  for  $0 \leq z \leq 2 \text{ nm}$ ,  $G(z) \cos \pi = -F(z) = -1$  for  $8 \leq z \leq 10 \text{ nm}$ , and  $G(z) = F(z) = 0$  elsewhere. (a2) Summed Hall conductance of the top two layers. (b2) Summed Hall conductance of the bottom two layers. Here,  $E_F = 0$ , and all other parameters are the same as in Fig. 2.

$k_x, k_y \in [-\pi, \pi] \text{ nm}^{-1}$ , and the Fermi energy  $E_F$  is assumed to lie within the energy gap of the surface states.

We further explore the dependence of the Hall conductance on the orientation  $\varphi$  of the external in-plane magnetic field in the case of the altermagnet-induced layer Hall effect. Figures 3(a1) and 3(b1) show the analytically calculated Hall conductances of the top and bottom surfaces, based on Eqs. (16) and (17), with the Fermi energy  $E_F$  lying within the surface gap. The sign of the half-quantized Hall conductance is tunable by varying  $\varphi$ , and the top and bottom surfaces exhibit opposite signs as expected for the layer Hall effect.

For comparison, the numerically evaluated summed Hall conductances of the top and bottom two layers at  $E_F = 0$  are plotted in Figs. 3(a2) and 3(b2), respectively. The numerical results are in good agreement with the analytical predictions, confirming the robustness of the altermagnet-induced layer Hall effect against variations in field orientation. Interestingly, the Hall conductance of the top (bottom) surface state exhibits periodic sign

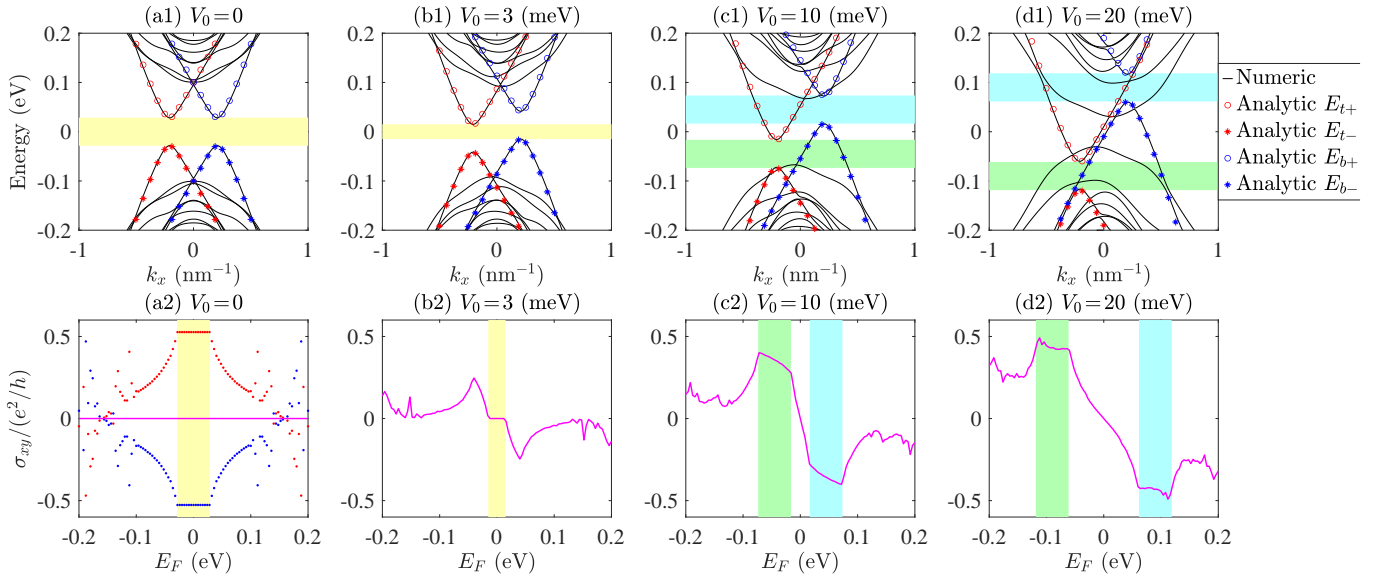


FIG. 4. Band structures and Hall conductances for the altermagnet-induced layer Hall effect under different strengths  $V_0$ , which could be induced by applying the perpendicular electric field. Upper row: [(a1)-(d1)] show the energy spectra for (a1)  $V_0 = 0$ , (b1)  $V_0 = 3$  meV, (c1)  $V_0 = 10$  meV, and (d1)  $V_0 = 20$  meV. Black curves show numerical results under OBCs along  $z$  direction and PBCs along  $x$  and  $y$  directions. Red (blue) circles and asterisks represent analytical surface-state spectra for the top (bottom) surface obtained from Eqs. (21) and (23). In (a1) and (b1), the yellow shaded region marks the bandwidth of the surface states, while in (c1) and (d1), the cyan (green) shaded regions indicate the bandwidths of the top (bottom) surface states. Lower row: [(a2)-(d2)] display the corresponding Hall conductance as a function of the Fermi energy  $E_F$ . Magenta lines show the total Hall conductance,  $\sigma_{xy} = \sum_{j_z} \sigma_{xy}(j_z)$ . In (a2), red (blue) dots denote the summed layer Hall conductance of the top (bottom) two layers. The system consists of a top altermagnetic layer ( $d_t = 2$  nm) and a bottom inverse altermagnetic layer ( $d_b = 2$  nm), with  $G(z) \cos 0 = F(z) = 1$  for  $0 \leq z \leq 2$  nm,  $G(z) \cos \pi = -F(z) = -1$  for  $8 \leq z \leq 10$  nm, and  $G(z) = F(z) = 0$  elsewhere. These parameters are identical to those used in Figs. 2(c1) and 2(c2). All other parameters are the same as those used in Fig. 2.

reversals at  $\varphi \approx \frac{(2n+1)\pi}{4}$  ( $n = 0, 1, 2, 3$ ).

## V. PERPENDICULAR ELECTRIC FIELD FOR LAYER HALL EFFECT

In this section, we demonstrate that the layer Hall effect becomes experimentally observable upon applying a perpendicular (out-of-plane) electric field  $E_z$  [1, 2].

We assume that the electric field  $E_z$  induces a potential  $\hat{V}(z)$  that is an odd function of the out-of-plane coordinate  $z$ , expressed as [1, 2]:

$$\hat{V}(z) = V_0 \left[ j_z - \frac{1}{2}(N_z + 1) \right] \sigma_0 \otimes \tau_0, \quad (18)$$

where  $V_0$  characterizes the layer-dependent potential induced by  $E_z$ , and  $j_z = 1, 2, 3, \dots, N_z$  indexes the individual layers with  $j_z = z/a_z$  and  $N_z = L_z/a_z$ . Here,  $L_z$  denotes the sample thickness along the  $z$  direction.

Incorporating this potential  $\hat{V}(z)$  into the real-space tight-binding Hamiltonian (7), the Dirac mass term in

Eq. (9) is modified as

$$\begin{aligned} \hat{M}(z) &= \hat{M}_0 + \hat{V}(z) \\ &= (M - 2t_z - 4t_{||}) \sigma_0 \otimes \tau_z \\ &\quad + F(z) (\Delta_x \sigma_y - \Delta_y \sigma_x) \otimes \tau_0 + \hat{V}(z). \end{aligned} \quad (19)$$

To analytically investigate the effect of  $E_z$  on the surface states, we derive the effective surface Hamiltonians for both the top and bottom surfaces.

On the basis of the potential  $\hat{V}(z)$ , i.e., Eq. (18), the effective Hamiltonian for the top surface state reads

$$\begin{aligned} \hat{\mathcal{H}}_{\text{sur}}^{\text{top}}(\mathbf{k}_{||}) &= -A_2 \left( k_y + \frac{\Delta_y}{A_2} \right) \sigma_x + A_2 \left( k_x + \frac{\Delta_x}{A_2} \right) \sigma_y \\ &\quad + J_{\text{top}}(k_x, k_y) \sigma_z + \frac{1}{2} (1 - N_z) V_0 \sigma_0 \otimes \tau_0. \end{aligned} \quad (20)$$

The corresponding eigenenergies for the top surface states are given by

$$\begin{aligned} E_{\text{sur}}^{\text{top}(\pm)}(\mathbf{k}_{||}) &= \frac{1}{2} (1 - N_z) V_0 \\ &\quad \pm \sqrt{A_2^2 [E_0^{\text{top}}(k_x, k_y)]^2 + [J_{\text{top}}(k_x, k_y)]^2}, \end{aligned} \quad (21)$$

where  $[E_0^{\text{top}}(k_x, k_y)]^2 = \left(k_y + \frac{\Delta_y}{A_2}\right)^2 + \left(k_x + \frac{\Delta_x}{A_2}\right)^2$ .

Furthermore, the effective Hamiltonian for the bottom surface state is evaluated as

$$\begin{aligned} \hat{\mathcal{H}}_{\text{sur}}^{\text{bot}}(\mathbf{k}_{||}) = & A_2 \left( k_y - \frac{\Delta_y}{A_2} \right) \sigma_x - A_2 \left( k_x - \frac{\Delta_x}{A_2} \right) \sigma_y \\ & + J_{\text{bot}}(k_x, k_y) \sigma_z + \frac{1}{2} (N_z - 1) V_0 \sigma_0 \otimes \tau_0. \end{aligned} \quad (22)$$

The corresponding eigenenergies for the bottom surface states are given by

$$\begin{aligned} E_{\text{sur}}^{\text{bot}(\pm)}(\mathbf{k}_{||}) = & \frac{1}{2} (N_z - 1) V_0 \\ & \pm \sqrt{A_2^2 [E_0^{\text{bot}}(k_x, k_y)]^2 + [J_{\text{bot}}(k_x, k_y)]^2}, \end{aligned} \quad (23)$$

where  $[E_0^{\text{bot}}(k_x, k_y)]^2 = \left(k_y - \frac{\Delta_y}{A_2}\right)^2 + \left(k_x - \frac{\Delta_x}{A_2}\right)^2$ .

As shown in Fig. 4, we numerically calculate the band structures and Hall conductances for the altermagnet-induced layer Hall effect under different strengths  $V_0$ , which could be induced by applying the perpendicular electric field.

By comparing Fig. 4(a1) and Fig. 4(b1), one observes that the bandwidth (yellow-shaded region) becomes significantly narrower upon applying a small electric field with  $V_0 = 3$  meV. In the absence of  $E_z$ , the total Hall conductance  $\sigma_{xy} = \sum_{j_z} \sigma_{xy}(j_z)$  (magenta curve) vanishes, as the opposite half-quantized layer Hall conductances from the top and bottom surfaces cancel each other [Fig. 4(a2)]. However, when  $E_z$  is applied, this cancellation only persists within the narrower yellow-shaded region [Fig. 4(b2)], whose width is determined by the gapped bandwidth. Outside this region, the total Hall conductance becomes finite.

As  $V_0$  increases further, the bulk gap gradually closes, lifting the exact cancellation between the two surfaces. The total Hall conductance then becomes finite and varies continuously with the Fermi energy  $E_F$ . Notably, two approximate plateaus appear, one positive (green) and one negative (cyan), as shown in Figs. 4(c1) and 4(d1). The positive plateau corresponds to the gap of the top surface states, while the negative one arises from the bottom surface states. The widths of these plateaus are determined by the respective surface-state bandwidths. The emergence of nonzero plateaus and peaks in the total Hall conductance thus provides clear and experimentally accessible signatures of the layer Hall effect.

To explore the tunability of the total Hall conductance with respect to the orientation  $\varphi$  of the external in-plane magnetic field and the perpendicular (out-of-plane) electric field, we plot the total Hall conductance as a function of  $\varphi$  and  $V_0$  at a fixed Fermi energy  $E_F = 10$  meV, as shown in Fig. 5. When  $V_0 = 0$ , the total Hall conductance vanishes identically for all  $\varphi$  due to the exact cancellation between the contributions from the top and

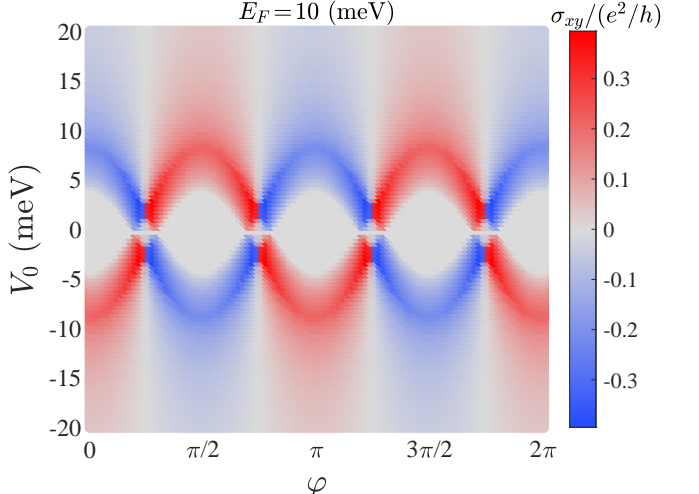


FIG. 5. Total Hall conductance as a function of  $\varphi$  and  $V_0$  at a fixed Fermi energy  $E_F = 10$  meV. The system consists of a top altermagnetic layer ( $d_t = 2$  nm) and a bottom inverse altermagnetic layer ( $d_b = 2$  nm). The spatial profiles are specified as  $G(z) \cos 0 = F(z) = 1$  for  $0 \leq z \leq 2$  nm,  $G(z) \cos \pi = -F(z) = -1$  for  $8 \leq z \leq 10$  nm, and  $G(z) = F(z) = 0$  elsewhere. These parameters are identical to those used in Figs. 2(c1) and 2(c2). All other parameters are the same as those used in Fig. 2.

bottom surface states. Upon applying a finite perpendicular electric field, this cancellation is lifted, giving rise to a finite Hall response. Particularly, the total Hall conductance undergoes periodic sign reversals at  $\varphi \approx \frac{(2n+1)\pi}{4}$  ( $n = 0, 1, 2, 3$ ), closely resembling the behavior of the individual surface Hall conductances shown in Fig. 3. Furthermore, when the electric field is applied symmetrically, i.e.,  $V_0 \in [-20, 20]$  meV, the total Hall conductance exhibits a  $\pi$ -periodic dependence on  $\varphi$ .

## VI. SUMMARY

In summary, we have proposed a scheme to realize the layer Hall effect in the ferromagnetic topological insulator  $\text{Bi}_2\text{Se}_3$  through proximity to  $d$ -wave altermagnets. We demonstrated that the combination of an altermagnet and an in-plane magnetic field gaps the surface Dirac cone, leading to an altermagnet-induced half-quantized Hall effect. When altermagnets with antiparallel Néel vectors are applied to the top and bottom surfaces, producing a layer Hall effect with vanishing net Hall conductance. By contrast, when altermagnets with parallel Néel vectors are applied, yielding a quantized Chern insulating state, i.e., the altermagnet-induced anomalous Hall effect.

We further showed that the Hall conductance depends sensitively on the orientation of the in-plane magnetic field, providing an additional degree of control over the topological response. Moreover, we demonstrated that

the layer Hall effect becomes experimentally observable upon applying a perpendicular electric field, which enables direct detection in realistic setups.

Taken together, these results establish a versatile framework for engineering altermagnet-induced topological phases in ferromagnetic topological insulators. Our findings not only deepen the understanding of altermagnetism in topological systems but also open avenues for the design and realization of altermagnet-based topological quantum materials.

## ACKNOWLEDGMENTS

R.C. acknowledges support from the National Natural Science Foundation of China (Grants No. 12304195 and U25D8012), the Chutian Scholars Program in Hubei Province, the Hubei Provincial Natural Science Foundation (Grant No. 2025AFA081), the Wuhan city key R&D program (under Grant No. 2025050602030069), and the Original Seed Program of Hubei University. F.Q. acknowledges support from the Jiangsu Specially-Appointed Professor Program in Jiangsu Province and the Doctoral Research Start-Up Fund of Jiangsu University of Science and Technology.

## DATA AVAILABILITY

The data are available from the authors upon reasonable request.

---

[1] Anyuan Gao, Yu-Fei Liu, Chaowei Hu, Jian-Xiang Qiu, Christian Tzschaschel, Barun Ghosh, Sheng-Chin Ho, Damien Bérbé, Rui Chen, Haipeng Sun, *et al.*, “Layer Hall effect in a 2D topological axion antiferromagnet,” *Nature* **595**, 521 (2021).

[2] Rui Chen, Hai-Peng Sun, Mingqiang Gu, Chun-Bo Hua, Qihang Liu, Hai-Zhou Lu, and XC Xie, “Layer Hall effect induced by hidden Berry curvature in antiferromagnetic insulators,” *National Science Review* **11**, nwac140 (2024).

[3] Ankita Anirban, “Quantum anomalous layer Hall effect,” *Nature Reviews Physics* **5**, 271 (2023).

[4] Wen-Bo Dai, Hailong Li, Dong-Hui Xu, Chui-Zhen Chen, and X. C. Xie, “Quantum anomalous layer Hall effect in the topological magnet  $\text{MnBi}_2\text{Te}_4$ ,” *Phys. Rev. B* **106**, 245425 (2022).

[5] Rui Peng, Ting Zhang, Zhonglin He, Qian Wu, Ying Dai, Baibiao Huang, and Yandong Ma, “Intrinsic layer-polarized anomalous Hall effect in bilayer  $\text{MnBi}_2\text{Te}_4$ ,” *Phys. Rev. B* **107**, 085411 (2023).

[6] Hong Xu, Xuqi Li, Haidan Sang, Yu Zhang, Wenying Mu, and Shifei Qi, “Layer-polarized anomalous Hall effect in the  $\text{MnBi}_2\text{Te}_4/\text{In}_2\text{Se}_3$  ( $\text{In}_2\text{Te}_3$ ) heterostructures,” *Materials Today Quantum* **3**, 100012 (2024).

[7] Chao Lei and Allan H. MacDonald, “Kerr, Faraday, and magnetoelectric effects in  $\text{MnBi}_2\text{Te}_4$  thin films,” *Phys. Rev. B* **108**, 125424 (2023).

[8] L. L. Tao, Qin Zhang, Huinan Li, Hong Jian Zhao, Xianjie Wang, Bo Song, Evgeny Y. Tsymbal, and Laurent Bellaiche, “Layer Hall Detection of the Néel Vector in Centrosymmetric Magnetoelectric Antiferromagnets,” *Phys. Rev. Lett.* **133**, 096803 (2024).

[9] Xiao-Xia Yi, Chun-Bo Hua, Rui Chen, and Bin Zhou, “Disorder-enhanced layer Hall effect in a magnetic sandwich heterostructure,” *Phys. Rev. B* **109**, 115301 (2024).

[10] Ting Zhang, Xilong Xu, Baibiao Huang, Ying Dai, Liangzhi Kou, and Yandong Ma, “Layer-polarized anomalous Hall effects in valleytronic van der Waals bilayers,” *Materials Horizons* **10**, 483 (2023).

[11] Ting Zhang, Xilong Xu, Jinghua Guo, Ying Dai, and Yandong Ma, “Layer-polarized anomalous Hall effects from inversion-symmetric single-layer lattices,” *Nano Letters* **24**, 1009 (2024).

[12] Yangyang Feng, Ying Dai, Baibiao Huang, Liangzhi Kou, and Yandong Ma, “Layer Hall effect in multiferroic two-dimensional materials,” *Nano Letters* **23**, 5367 (2023).

[13] Yibo Liu, Yangyang Feng, Ying Dai, Baibiao Huang, and Yandong Ma, “Engineering layertronics in two-dimensional ferromagnetic multiferroic lattice,” *Nano Letters* **24**, 3507 (2024).

[14] Yulei Han, Yunpeng Guo, Zeyu Li, and Zhenhua Qiao, “Layer Hall Effect without External Electric Field,” *Phys. Rev. Lett.* **134**, 236206 (2025).

[15] Jing Wang, Biao Lian, Xiao-Liang Qi, and Shou-Cheng Zhang, “Quantized topological magnetoelectric effect of the zero-plateau quantum anomalous Hall state,” *Phys. Rev. B* **92**, 081107 (2015).

[16] Takahiro Morimoto, Akira Furusaki, and Naoto Nagaosa, “Topological magnetoelectric effects in thin films of topological insulators,” *Phys. Rev. B* **92**, 085113 (2015).

[17] M Mogi, M Kawamura, R Yoshimi, A Tsukazaki, Y Kozuka, N Shirakawa, KS Takahashi, M Kawasaki, and Y Tokura, “A magnetic heterostructure of topological insulators as a candidate for an axion insulator,” *Nature materials* **16**, 516 (2017).

[18] Masataka Mogi, Minoru Kawamura, Atsushi Tsukazaki, Ryutaro Yoshimi, Kei S Takahashi, Masashi Kawasaki, and Yoshinori Tokura, “Tailoring tricolor structure of magnetic topological insulator for robust axion insulator,” *Science advances* **3**, eaao1669 (2017).

[19] Nicodemos Varnava and David Vanderbilt, “Surfaces of axion insulators,” *Phys. Rev. B* **98**, 245117 (2018).

[20] Di Xiao, Jue Jiang, Jae-Ho Shin, Wenbo Wang, Fei Wang, Yi-Fan Zhao, Chaoxing Liu, Weida Wu, Moses H. W. Chan, Nitin Samarth, and Cui-Zu Chang, “Realization of the Axion Insulator State in Quantum Anomalous Hall Sandwich Heterostructures,” *Phys. Rev. Lett.* **120**, 056801 (2018).

[21] Yuanfeng Xu, Zhida Song, Zhijun Wang, Hongming Weng, and Xi Dai, “Higher-Order Topology of the Axion Insulator EuIn<sub>2</sub>As<sub>2</sub>,” *Phys. Rev. Lett.* **122**, 256402 (2019).

[22] Dongqin Zhang, Minji Shi, Tongshuai Zhu, Dingyu Xing, Haijun Zhang, and Jing Wang, “Topological Axion States in the Magnetic Insulator MnBi<sub>2</sub>Te<sub>4</sub> with the Quantized Magnetoelectric Effect,” *Phys. Rev. Lett.* **122**, 206401 (2019).

[23] Chang Liu, Yongchao Wang, Hao Li, Yang Wu, Yaxin Li, Jiaheng Li, Ke He, Yong Xu, Jinsong Zhang, and Yanyu Wang, “Robust axion insulator and Chern insulator phases in a two-dimensional antiferromagnetic topological insulator,” *Nature materials* **19**, 522 (2020).

[24] Dennis M Nenno, Christina AC Garcia, Johannes Gooth, Claudia Felser, and Prineha Narang, “Axion physics in condensed-matter systems,” *Nature Reviews Physics* **2**, 682 (2020).

[25] Shuai Li, Ming Gong, Shuguang Cheng, Hua Jiang, and XC Xie, “Dissipationless layertronics in axion insulator MnBi<sub>2</sub>Te<sub>4</sub>,” *National Science Review* **11**, nwad262 (2024).

[26] Fang Qin, Ching Hua Lee, and Rui Chen, “Light-induced half-quantized Hall effect and axion insulator,” *Phys. Rev. B* **108**, 075435 (2023).

[27] Shuai Li, Ming Gong, Yu-Hang Li, Hua Jiang, and XC Xie, “High spin axion insulator,” *Nature communications* **15**, 4250 (2024).

[28] Congjun Wu and Shou-Cheng Zhang, “Dynamic Generation of Spin-Orbit Coupling,” *Phys. Rev. Lett.* **93**, 036403 (2004).

[29] Congjun Wu, Kai Sun, Eduardo Fradkin, and Shou-Cheng Zhang, “Fermi liquid instabilities in the spin channel,” *Phys. Rev. B* **75**, 115103 (2007).

[30] Satoru Hayami, Yuki Yanagi, and Hiroaki Kusunose, “Momentum-dependent spin splitting by collinear antiferromagnetic ordering,” *Journal of the Physical Society of Japan* **88**, 123702 (2019).

[31] Satoru Hayami, Yuki Yanagi, and Hiroaki Kusunose, “Bottom-up design of spin-split and reshaped electronic band structures in antiferromagnets without spin-orbit coupling: Procedure on the basis of augmented multipoles,” *Phys. Rev. B* **102**, 144441 (2020).

[32] Libor Šmejkal, Anna Birk Hellenes, Rafael González-Hernández, Jairo Sinova, and Tomas Jungwirth, “Giant and Tunneling Magnetoresistance in Unconventional Collinear Antiferromagnets with Nonrelativistic Spin-Momentum Coupling,” *Phys. Rev. X* **12**, 011028 (2022).

[33] Libor Šmejkal, Jairo Sinova, and Tomas Jungwirth, “Beyond Conventional Ferromagnetism and Antiferromagnetism: A Phase with Nonrelativistic Spin and Crystal Rotation Symmetry,” *Phys. Rev. X* **12**, 031042 (2022).

[34] Libor Šmejkal, Jairo Sinova, and Tomas Jungwirth, “Emerging Research Landscape of Altermagnets,” *Phys. Rev. X* **12**, 040501 (2022).

[35] Yu-Xin Li, Yiyuan Chen, Liqing Pan, Shuai Li, Song-Bo Zhang, and Hai-Zhou Lu, “Exploration of altermagnetism in RuO<sub>2</sub>,” (2025).

[36] Kyo-Hoon Ahn, Atsushi Hariki, Kwan-Woo Lee, and Jan Kuneš, “Antiferromagnetism in RuO<sub>2</sub> as *d*-wave Pomeranchuk instability,” *Phys. Rev. B* **99**, 184432 (2019).

[37] Libor Šmejkal, Rafael González-Hernández, Tomáš Jungwirth, and Jairo Sinova, “Crystal time-reversal symmetry breaking and spontaneous Hall effect in collinear antiferromagnets,” *Science advances* **6**, eaaz8809 (2020).

[38] Ding-Fu Shao, Shu-Hui Zhang, Ming Li, Chang-Beom Eom, and Evgeny Y Tsymbal, “Spin-neutral currents for spintronics,” *Nature Communications* **12**, 7061 (2021).

[39] Rafael González-Hernández, Libor Šmejkal, Karel Výborný, Yuta Yahagi, Jairo Sinova, Tomáš Jungwirth, and Jakub Železný, “Efficient Electrical Spin Splitter Based on Nonrelativistic Collinear Antiferromagnetism,” *Phys. Rev. Lett.* **126**, 127701 (2021).

[40] Arnab Bose, Nathaniel J Schreiber, Rakshit Jain, Ding-Fu Shao, Hari P Nair, Jiaxin Sun, Xiyue S Zhang, David A Muller, Evgeny Y Tsymbal, Darrell G Schlom, *et al.*, “Tilted spin current generated by the collinear antiferromagnet ruthenium dioxide,” *Nature Electronics* **5**, 267 (2022).

[41] H. Bai, L. Han, X. Y. Feng, Y. J. Zhou, R. X. Su, Q. Wang, L. Y. Liao, W. X. Zhu, X. Z. Chen, F. Pan, X. L. Fan, and C. Song, “Observation of Spin Splitting Torque in a Collinear Antiferromagnet RuO<sub>2</sub>,” *Phys. Rev. Lett.* **128**, 197202 (2022).

[42] Shutaro Karube, Takahiro Tanaka, Daichi Sugawara, Naohiro Kadoguchi, Makoto Kohda, and Junsaku Nitta, “Observation of Spin-Splitter Torque in Collinear Antiferromagnetic RuO<sub>2</sub>,” *Phys. Rev. Lett.* **129**, 137201 (2022).

[43] Cong He, Zhenchao Wen, Jun Okabayashi, Yoshio Miura, Tianyi Ma, Tadakatsu Ohkubo, Takeshi Seki, Hiroaki Sukegawa, and Seiji Mitani, “Evidence for single variant in altermagnetic RuO<sub>2</sub> (101) thin films,” *Nature Communications* **16**, 8235 (2025).

[44] Marko Milivojević, Marko Orozović, Silvia Picozzi, Martin Gmitra, and Srdan Stavrić, “Interplay of altermagnetism and weak ferromagnetism in two-dimensional RuF<sub>4</sub>,” *2D Materials* **11**, 035025 (2024).

[45] Atasi Chakraborty, Rafael González Hernández, Libor Šmejkal, and Jairo Sinova, “Strain-induced phase transition from antiferromagnet to altermagnet,” *Phys. Rev. B* **109**, 144421 (2024).

[46] Sayantika Bhowal and Nicola A. Spaldin, “Ferroically Ordered Magnetic Octupoles in *d*-Wave Altermagnets,” *Phys. Rev. X* **14**, 011019 (2024).

[47] Yu-Xuan Li, Yichen Liu, and Cheng-Cheng Liu, “Creation and manipulation of higher-order topological states by altermagnets,” *Phys. Rev. B* **109**, L201109 (2024).

[48] Igor I Mazin, Klaus Koepernik, Michelle D Johannes, Rafael González-Hernández, and Libor Šmejkal, “Prediction of unconventional magnetism in doped FeSb<sub>2</sub>,” *Proceedings of the National Academy of Sciences* **118**, e2108924118 (2021).

[49] Lotan Attias, Alex Levchenko, and Maxim Khodas, “Intrinsic anomalous Hall effect in altermagnets,” *Phys. Rev. B* **110**, 094425 (2024).

[50] Cole Phillips, Ganesh Pokharel, Kyryl Shtefienko, Shalika R. Bhandari, David E. Graf, D. P. Rai, and Keshav Shrestha, “Electronic structure of the altermagnet candidate  $\text{FeSb}_2$ : High-field torque magnetometry and density functional theory studies,” *Phys. Rev. B* **111**, 075141 (2025).

[51] Sonka Reimers, Lukas Odenbreit, Libor Šmejkal, Vladimir N Strocov, Prokopios Constantinou, Anna B Hellenes, Rodrigo Jaeschke Ubiergo, Warley H Campos, Venkata K Bharadwaj, Atasi Chakraborty, *et al.*, “Direct observation of altermagnetic band splitting in  $\text{CrSb}$  thin films,” *Nature Communications* **15**, 2116 (2024).

[52] Jianyang Ding, Zhicheng Jiang, Xiuhua Chen, Zicheng Tao, Zhengtai Liu, Tongrui Li, Jishan Liu, Jianping Sun, Jinguang Cheng, Jiayu Liu, Yichen Yang, Runfeng Zhang, Liwei Deng, Wenchuan Jing, Yu Huang, Yuming Shi, Mao Ye, Shan Qiao, Yilin Wang, Yanfeng Guo, Donglai Feng, and Dawei Shen, “Large Band Splitting in  $g$ -Wave Altermagnet  $\text{CrSb}$ ,” *Phys. Rev. Lett.* **133**, 206401 (2024).

[53] Xin Peng, Yuzhi Wang, Shengnan Zhang, Yi Zhou, Yuran Sun, Yahui Su, Chunxiang Wu, Tingyu Zhou, Le Liu, Hangdong Wang, Jinhua Yang, Bin Chen, Zhong Fang, Jianhua Du, Zhiwei Jiao, Quansheng Wu, and Minghu Fang, “Scaling behavior of magnetoresistance and Hall resistivity in the altermagnet  $\text{CrSb}$ ,” *Phys. Rev. B* **111**, 144402 (2025).

[54] Zhiyuan Zhou, Xingkai Cheng, Mengli Hu, Ruiyue Chu, Hua Bai, Lei Han, Junwei Liu, Feng Pan, and Cheng Song, “Manipulation of the altermagnetic order in  $\text{CrSb}$  via crystal symmetry,” *Nature* **638**, 645 (2025).

[55] I. I. Mazin, “Altermagnetism in  $\text{MnTe}$ : Origin, predicted manifestations, and routes to detwinning,” *Phys. Rev. B* **107**, L100418 (2023).

[56] J Krempaský, L Šmejkal, SW D’souza, M Hajlaoui, G Springholz, K Uhlířová, F Alarab, PC Constantinou, V Strocov, D Usanov, *et al.*, “Altermagnetic lifting of Kramers spin degeneracy,” *Nature* **626**, 517 (2024).

[57] Suyoung Lee, Sangjae Lee, Saegyeol Jung, Jiwon Jung, Donghan Kim, Yeonjae Lee, Byeongjun Seok, Jaeyoung Kim, Byeong Gyu Park, Libor Šmejkal, Chang-Jong Kang, and Changyoung Kim, “Broken Kramers Degeneracy in Altermagnetic  $\text{MnTe}$ ,” *Phys. Rev. Lett.* **132**, 036702 (2024).

[58] T. Osumi, S. Souma, T. Aoyama, K. Yamauchi, A. Honma, K. Nakayama, T. Takahashi, K. Ohgushi, and T. Sato, “Observation of a giant band splitting in altermagnetic  $\text{MnTe}$ ,” *Phys. Rev. B* **109**, 115102 (2024).

[59] N. N. Orlova, V. D. Esin, A. V. Timonina, N. N. Kolesnikov, and E. V. Deviatov, “Magnetocaloric effect for the altermagnetic candidate  $\text{MnTe}$ ,” *arXiv:2510.02777* (2025).

[60] Miina Leiviskä, Javier Rial, Antonín Bad’ura, Rafael Lopes Seeger, Ismaïla Kounta, Sebastian Beckert, Dominik Kriegner, Isabelle Joumard, Eva Schmoranzerová, Jairo Sinova, Olena Gomonay, Andy Thomas, Sebastian T. B. Goennenwein, Helena Reichlová, Libor Šmejkal, Lisa Michez, Tomáš Jungwirth, and Vincent Baltz, “Anisotropy of the anomalous Hall effect in thin films of the altermagnet candidate  $\text{Mn}_5\text{Si}_3$ ,” *Phys. Rev. B* **109**, 224430 (2024).

[61] Helena Reichlova, Rafael Lopes Seeger, Rafael González-Hernández, Ismaila Kounta, Richard Schlitz, Dominik Kriegner, Philipp Ritzinger, Michaela Lammel, Miina Leiviskä, Anna Birk Hellenes, *et al.*, “Observation of a spontaneous anomalous Hall response in the  $\text{Mn}_5\text{Si}_3$   $d$ -wave altermagnet candidate,” *Nature Communications* **15**, 4961 (2024).

[62] Javier Rial, Miina Leiviskä, Gregor Skobjin, Antonín Bad’ura, Gilles Gaudin, Florian Disdier, Richard Schlitz, Ismaïla Kounta, Sebastian Beckert, Dominik Kriegner, Andy Thomas, Eva Schmoranzerová, Libor Šmejkal, Jairo Sinova, Tomáš Jungwirth, Lisa Michez, Helena Reichlová, Sebastian T. B. Goennenwein, Olena Gomonay, and Vincent Baltz, “Altermagnetic variants in thin films of  $\text{Mn}_5\text{Si}_3$ ,” *Phys. Rev. B* **110**, L220411 (2024).

[63] Lorenzo Vistoli, Wenbo Wang, Anke Sander, Qiuxiang Zhu, Blai Casals, Rafael Cicheler, Agnès Barthélémy, Stéphane Fusil, Gervasi Herranz, Sergio Valencia, *et al.*, “Giant topological Hall effect in correlated oxide thin films,” *Nature Physics* **15**, 67 (2019).

[64] Rafael M. Fernandes, Vanuildo S. de Carvalho, Turan Birol, and Rodrigo G. Pereira, “Topological transition from nodal to nodeless Zeeman splitting in altermagnets,” *Phys. Rev. B* **109**, 024404 (2024).

[65] Bei Jiang, Mingzhe Hu, Jianli Bai, Ziyin Song, Chao Mu, Gexing Qu, Wan Li, Wenliang Zhu, Hanqi Pi, Zhongxu Wei, *et al.*, “A metallic room-temperature  $d$ -wave altermagnet,” *Nature Physics* **21**, 754 (2025).

[66] Rajib Sarkar, “Altermagnet with a metallic touch,” *Nature Physics* **21**, 691 (2025).

[67] Hao-Jie Lin, Song-Bo Zhang, Hai-Zhou Lu, and X. C. Xie, “Coulomb Drag in Altermagnets,” *Phys. Rev. Lett.* **134**, 136301 (2025).

[68] Yiyuan Chen, Xiaoxiong Liu, Hai-Zhou Lu, and X. C. Xie, “Electrical switching of altermagnetism,” *Phys. Rev. Lett.* **135**, 016701 (2025).

[69] Rui Chen, Zi-Ming Wang, Ke Wu, Hai-Peng Sun, Bin Zhou, Rui Wang, and Dong-Hui Xu, “Probing  $k$ -Space Alternating Spin Polarization via the Anomalous Hall Effect,” *Phys. Rev. Lett.* **135**, 096602 (2025).

[70] Zi-Ming Wang, Yang Zhang, Song-Bo Zhang, Jin-Hua Sun, Elbio Dagotto, Dong-Hui Xu, and Lun-Hui Hu, “Spin-Orbital Altermagnetism,” *Phys. Rev. Lett.* **135**, 176705 (2025).

[71] Jabir Ali Ouassou, Arne Brataas, and Jacob Linder, “dc Josephson Effect in Altermagnets,” *Phys. Rev. Lett.* **131**, 076003 (2023).

[72] Qiang Cheng and Qing-Feng Sun, “Orientation-dependent josephson effect in spin-singlet superconductor/altermagnet/spin-triplet superconductor junctions,” *Phys. Rev. B* **109**, 024517 (2024).

[73] C. W. J. Beenakker and T. Vakhtel, “Phase-shifted Andreev levels in an altermagnet Josephson junction,” *Phys. Rev. B* **108**, 075425 (2023).

[74] Bo Lu, Kazuki Maeda, Hiroyuki Ito, Keiji Yada, and Yukio Tanaka, “ $\varphi$  Josephson Junction Induced by Altermagnetism,” *Phys. Rev. Lett.* **133**, 226002 (2024).

[75] Hai-Peng Sun, Song-Bo Zhang, Chang-An Li, and Björn Trauzettel, “Tunable second harmonic in altermagnetic Josephson junctions,” *Phys. Rev. B* **111**, 165406 (2025).

[76] Chi Sun, Arne Brataas, and Jacob Linder, “Andreev reflection in altermagnets,” *Phys. Rev. B* **108**, 054511 (2023).

[77] Michal Papaj, “Andreev reflection at the altermagnet-superconductor interface,” *Phys. Rev. B* **108**, L060508 (2023).

[78] Yuan Fang, Jennifer Cano, and Sayed Ali Akbar Ghorashi, “Quantum Geometry Induced Nonlinear Transport in Altermagnets,” *Phys. Rev. Lett.* **133**, 106701 (2024).

[79] Tian-Xin Liu, Fu-Yang Chen, Xin Xiao, Hou-Jian Duan, Rui-Qiang Wang, and Ming-Xun Deng, “Enhancement of the linear and nonlinear planar Hall effect by altermagnets on the surface of topological insulators,” *Phys. Rev. B* **111**, 155124 (2025).

[80] Yu-Fei Sun, Yue Mao, Yu-Chen Zhuang, and Qing-Feng Sun, “Tunneling magnetoresistance effect in altermagnets,” *Phys. Rev. B* **112**, 094411 (2025).

[81] Yu-Hao Wan and Qing-Feng Sun, “Altermagnetism-induced parity anomaly in weak topological insulators,” *Phys. Rev. B* **111**, 045407 (2025).

[82] Yu-Hao Wan, Peng-Yi Liu, and Qing-Feng Sun, “Interplay of altermagnetic order and Wilson mass in the Dirac equation: Helical edge states without time-reversal symmetry,” *Phys. Rev. B* **112**, 115412 (2025).

[83] Rui Chen, Bin Zhou, and Dong-Hui Xu, “Quasicrystalline Altermagnetism,” [arXiv:2507.18408](https://arxiv.org/abs/2507.18408) (2025).

[84] Zhi-Yan Shao, Chen Lu, Zhiming Pan, Yu-Bo Liu, and Fan Yang, “Classification of Magnetism and Altermagnetism in Quasicrystals,” [arXiv:2508.15702](https://arxiv.org/abs/2508.15702) (2025).

[85] Yiming Li, Mingxiang Pan, Jun Leng, Yuxiao Chen, and Huaqing Huang, “Unconventional Altermagnetism in Quasicrystals: A Hyperspatial Projective Construction,” [arXiv:2508.01564](https://arxiv.org/abs/2508.01564) (2025).

[86] Ding-Fu Shao, Yuan-Yuan Jiang, Jun Ding, Shu-Hui Zhang, Zi-An Wang, Rui-Chun Xiao, Gautam Gurung, W. J. Lu, Y. P. Sun, and Evgeny Y. Tsymbal, “Néel Spin Currents in Antiferromagnets,” *Phys. Rev. Lett.* **130**, 216702 (2023).

[87] Peng Rao, Alexander Mook, and Johannes Knolle, “Tunable band topology and optical conductivity in altermagnets,” *Phys. Rev. B* **110**, 024425 (2024).

[88] Hai-Yang Ma and Jin-Feng Jia, “Altermagnetic topological insulator and the selection rules,” *Phys. Rev. B* **110**, 064426 (2024).

[89] Daniil S. Antonenko, Rafael M. Fernandes, and Jörn W. F. Venderbos, “Mirror Chern Bands and Weyl Nodal Loops in Altermagnets,” *Phys. Rev. Lett.* **134**, 096703 (2025).

[90] Shuai Qu, Xiao-Yao Hou, Zheng-Xin Liu, Peng-Jie Guo, and Zhong-Yi Lu, “Altermagnetic Weyl node-network metals protected by spin symmetry,” *Phys. Rev. B* **111**, 195138 (2025).

[91] Kirill Parshukov, Raymond Wiedmann, and Andreas P. Schnyder, “Topological crossings in two-dimensional altermagnets: Symmetry classification and topological responses,” *Phys. Rev. B* **111**, 224406 (2025).

[92] Yang-Yang Li and Song-Bo Zhang, “Floating edge bands in the Bernevig-Hughes-Zhang model with altermagnetism,” *Phys. Rev. B* **111**, 045106 (2025).

[93] Zheng-Yang Zhuang, Di Zhu, Dongling Liu, Zhigang Wu, and Zhongbo Yan, “Odd-Parity Altermagnetism Originated from Orbital Orders,” [arXiv:2508.18361](https://arxiv.org/abs/2508.18361) (2025).

[94] Shengpu Huang, Zheng Qin, Fangyang Zhan, Dong-Hui Xu, Da-Shuai Ma, and Rui Wang, “Light-induced Odd-parity Magnetism in Conventional Collinear Antiferromagnets,” [arXiv:2507.20705](https://arxiv.org/abs/2507.20705) (2025).

[95] Tongshuai Zhu, Di Zhou, Huaiqiang Wang, and Jiawei Ruan, “Floquet odd-parity collinear magnets,” [arXiv:2508.02542](https://arxiv.org/abs/2508.02542) (2025).

[96] Dongling Liu, Zheng-Yang Zhuang, Di Zhu, Zhigang Wu, and Zhongbo Yan, “Light-induced odd-parity altermagnets on dimerized lattices,” [arXiv:2508.18360](https://arxiv.org/abs/2508.18360) (2025).

[97] Jiong-Yi Zhu, Zheng-Rong Liu, Rui Chen, and Bin Zhou, “Floquet-induced two-dimensional weak topological insulator phase,” *Phys. Rev. B* **112**, 115436 (2025).

[98] Bo Fu, Chang-An Li, and Björn Trauzettel, “Altermagnetism Induced Bogoliubov Fermi Surfaces Form Topological Superconductivity,” [arXiv:2512.20049](https://arxiv.org/abs/2512.20049) (2025).

[99] Chao-Xing Liu, Xiao-Liang Qi, HaiJun Zhang, Xi Dai, Zhong Fang, and Shou-Cheng Zhang, “Model Hamiltonian for topological insulators,” *Phys. Rev. B* **82**, 045122 (2010).

[100] Haijun Zhang, Chao-Xing Liu, Xiao-Liang Qi, Xi Dai, Zhong Fang, and Shou-Cheng Zhang, “Topological insulators in  $\text{Bi}_2\text{Se}_3$ ,  $\text{Bi}_2\text{Te}_3$  and  $\text{Sb}_2\text{Te}_3$  with a single Dirac cone on the surface,” *Nature physics* **5**, 438 (2009).

[101] Cui-Zu Chang, Jinsong Zhang, Xiao Feng, Jie Shen, Zuocheng Zhang, Minghua Guo, Kang Li, Yunbo Ou, Pang Wei, Li-Li Wang, *et al.*, “Experimental observation of the quantum anomalous Hall effect in a magnetic topological insulator,” *Science* **340**, 167 (2013).

[102] M Mogi, Y Okamura, M Kawamura, R Yoshimi, K Yasuda, A Tsukazaki, KS Takahashi, T Morimoto, N Nagaosa, M Kawasaki, *et al.*, “Experimental signature of the parity anomaly in a semi-magnetic topological insulator,” *Nature Physics* **18**, 390 (2022).

[103] Jin-Yu Zou, Rui Chen, Bo Fu, Huan-Wen Wang, Zi-Ang Hu, and Shun-Qing Shen, “Half-quantized Hall effect at the parity-invariant Fermi surface,” *Phys. Rev. B* **107**, 125153 (2023).

[104] Fang Qin, Rui Chen, and Hai-Zhou Lu, “Phase transitions in intrinsic magnetic topological insulator with high-frequency pumping,” *Journal of Physics: Condensed Matter* **34**, 225001 (2022).

[105] Vladimir A. Zyuzin, “In-plane Hall effect in two-dimensional helical electron systems,” *Phys. Rev. B* **102**, 241105 (2020).

[106] Rui Yu, Wei Zhang, Hai-Jun Zhang, Shou-Cheng Zhang, Xi Dai, and Zhong Fang, “Quantized anomalous Hall effect in magnetic topological insulators,” *science* **329**, 61 (2010).

[107] Abhinav Kandala, Anthony Richardella, Susan Kempinger, Chao-Xing Liu, and Nitin Samarth, “Giant anisotropic magnetoresistance in a quantum anomalous Hall insulator,” *Nature communications* **6**, 7434 (2015).

[108] Supplemental Materials.